

MULTIWAVELENGTH OBSERVATIONS OF EXO 0748–676 – II. EMISSION LINE BEHAVIOR

K. J. PEARSON¹, R. I. HYNES¹, D. STEEGHS², P. G. JONKER^{3,4,5}, C. A. HASWELL⁶, A. R. KING⁷,

K. O'BRIEN⁸, G. NELEMANS⁹, M. MÉNDEZ³
Draft version September 26, 2018

ABSTRACT

We present optical and ultraviolet spectra, lightcurves, and Doppler tomograms of the low-mass X-ray binary EXO 0748–676. Using an extensive set of 15 emission line tomograms, we show that, along with the usual emission from the stream and “hot spot”, there is extended non-axisymmetric emission from the disk rim. Some of the emission and H α and β absorption features lend weight to the hypothesis that part of the stream overflows the disk rim and forms a two phase medium. The data are consistent with a 1.35M_⊙ neutron star with a main sequence companion and hence a mass ratio $q \approx 0.34$.

Subject headings: accretion, accretion disks—binaries: close – stars: individual: UY Vol

1. INTRODUCTION

The low-mass X-ray binary (LMXB) EXO 0748–676 was first recognised as a transient X-ray source by EXOSAT in 1985 (Parmar et al. 1985) and an optical counterpart, UY Vol, was soon associated with it (Wade et al. 1985). Rather than returning to a quiescent state, the system has persisted in outburst since then and fits the typical pattern of the “persistent” class of objects; showing extended periods of activity lasting several years before switching off for a similar period (White, Nasage & Parmar 1995). This intriguing behavior suggests that such systems are switching between two metastable states in an analogous situation to the Z Cam subgroup of the Dwarf Nova (DN) group of Cataclysmic Variables (CVs).

The outbursting behavior of DNe can be understood in terms of the accretion disk in the system being able to exist in two states (“hot” and “cold”) characterised by high (or conversely low) ionization, viscosity, mass throughput and luminosity (see, for example, the review of Warner 1995). Systems switch from the low state to the high at a critical surface density (or equivalently temperature) giving rise to high luminosity outbursts. Due to an hysteresis effect, the disk switches back to the low viscosity state at a second, lower, critical surface density and the disk then refills with material from the secondary. Z Cam stars exhibit “standstills” where outbursts are suspended. During these periods, the disk is maintained in a high-viscosity state. Transient LMXBs can be seen as the analogues of DNe with the central white dwarf replaced by a neutron star or black hole (see, for example, the review of King 2006). The model above must be modified to account for the effects of X-ray irradiation. This will tend to stabilise systems in the high state by reducing the critical mass-

transfer rate for transition back to the low state and thus lengthen the duration of outbursts (van Paradijs 1996; King, Kolb & Szuszkiewicz 1997). Like Z Cam stars, the persistent LMXB systems have a sufficient mass transfer rate to maintain extended periods of high luminosity, and the smaller size of the system makes this, rather than the low state, the default configuration. Occasionally (in evolutionary terms), they transition to a low viscosity state.

The review of King (2006) explains how the observed luminosity of EXO 0748–676 implies that the neutron star has accreted $\sim 10^{22}$ kg since the “turn-on” in 1985. Given that the maximum disk mass that would have allowed the disk to exist in the low state is $\sim 1.3 \times 10^{21}$ kg, this confirms that the system must currently be accreting in a *stable* “hot” configuration. The periods of reduced mass-transfer might plausibly be ascribed to starspots on the secondary (King & Cannizzo 1998).

Systems like EXO 0748–676 hold out the prospect of allowing us to probe the nature of the (in)stability mechanism. The understanding gained could then be transferred to more volatile systems.

EXO 0748–676 has an inclination that is well-constrained by its lightcurve. The inclination must be high enough that the disk rim can generate the X-ray dips and eclipses that are observed to recur on the 3.82 hr orbital period. On the other hand, it must also be low enough that the X-ray eclipse is sharp and brief, indicating that the neutron star is visible outside of eclipse. Quantitatively, this translates to the range $75^\circ < i < 82^\circ$ (Parmar et al. 1986; Hynes et al. 2006a). There is 4% residual X-ray flux during eclipse attributed to scattered emission by a small optically thin Accretion Disk Corona (ADC) (Parmar et al. 1986).

Probably the most natural place to seek the origin of

¹ Department of Physics and Astronomy, 202 Nicholson Hall, Louisiana State University, Baton Rouge, LA 70803, USA

² Harvard-Smithsonian Center for Astrophysics, 60 Garden Street, MS 67, MA 02138, Cambridge, U.S.A.

³ SRON - National Institute for Space Research, Sorbonnelaan 2, 3584 CA, Utrecht, The Netherlands

⁴ Harvard-Smithsonian Center for Astrophysics, 60 Garden Street, MS 83, MA 02138, Cambridge, U.S.A.

⁵ Astronomical Institute, Utrecht University, PO Box 80000, 3508 TA, Utrecht, The Netherlands

⁶ Department of Physics and Astronomy, The Open University, Walton Hall, Milton Keynes, MK7 6AA, UK

⁷ Department of Physics and Astronomy, The University of Leicester, University Road, Leicester, LE1 7RH, UK

⁸ European Southern Observatory, Casilla 19001, Santiago 19, Chile

⁹ Department of Astrophysics, Radboud University, PO Box 9010, 6500 GL, Nijmegen, The Netherlands

the dips is the disk rim. Analysis of the gas dynamics (Flannery 1975; Lubow & Shu 1975, 1976) indicate that the impact of the mass-transfer stream on the disk will cause a thickening of the rim. Following the suggestion of Mason et al. (1980), modelling of the X-ray lightcurve of 2A 1822-371 (White & Holt 1982) supported the need for such a rim structure. However, work by Frank, King & Lasota (1987) suggested that the absorbing material might actually be closer to the primary from material overflowing the disk rim. Simulations by Armitage & Livio (1996) showed that the interaction of the stream and disk did not produce enough disk thickening to prevent material flowing above and below the disk hot-spot, following a near-parabolic path and impacting at a locus of points across the disk face. This absorbing material would exist in a two-phase state as a result of an ionization instability: cool neutral clouds would coexist with a hot, ionized inter-cloud medium (Frank, King & Lasota 1987). The crucial difference between the two models is the relative thickness of the stream and disk. In a model that considers only gravity and gas pressure, the stream will spread to have a vertical height larger than the disk and would be expected to be able to flow over the disk surface. The disk would only exhibit a limited thickening downstream from the hotspot. In contrast, the contemporary incarnation of the thick rim model invokes X-ray irradiation to heat the disk rim and cause it to puff up. In this case, the stream would be unable to significantly overflow the disk. However, this picture suffers from the difficulty that to puff up the disk to a suitable height would require X-ray temperatures in the disk mid-plane. X-ray irradiation could only achieve this if the disk were optically thin to X-rays but, if this were so, the rim would not be able to act to obscure X-rays and cause dips.

We are aware of Doppler tomograms having previously been published for 7 X-ray binaries in a high state: 2A 1822-371 (Harlaftis, Charles & Horne 1997), Her X-1 (Still et al. 1997; Vrtilik et al. 2001), XTE J2123-058 (Hynes et al. 2001), Sco X-1 (Steeghs & Casares 2002), Cen X-4 (Torres et al. 2002; D’Avanzo et al. 2005), AC211 (Torres, Callanan & Garcia 2003) and XTE J1118+480 (Torres et al. 2004). This work presents a detailed study as part of a multiwavelength campaign using *HST*, *RXTE*, CTIO and Gemini with contemporaneous VLT and Magellan observations. In Paper I (Hynes et al. 2006a), we studied the burst properties of EXO 0748-676 using rapid spectroscopic and photometric data. Here, we study the accretion structure using spectra, lightcurves and Doppler tomograms from several optical and ultraviolet observations.

2. OBSERVATIONS

2.1. *HST*

Hubble Space Telescope (*HST*) observations of EXO 0748-676 were obtained on 2003 Feb 18–19 using the Space Telescope Imaging Spectrograph (STIS; Proffitt et al. 2002). The observations were timed such that the target was within the continuous viewing zone (CVZ). Consequently, we were able to observe over about 9 hrs with only small gaps for wavelength calibrations and mode

changes. This covered two complete binary orbits. Our coverage is summarised in Table 1.

All observations used the MAMA UV detectors in TIMETAG mode, yielding a stream of detected events with $125\ \mu\text{s}$ precision, which could be used to reconstruct spectra for any desired time-interval. Most observations concentrated on the far-UV, using the G140L grating. Two short observations of the near-UV region, using the G230L grating, were also obtained.

The G140L grating observations had a spectral dispersion of $0.6\ \text{\AA}/\text{pixel}$ which, combined with a resolution element varying with wavelength, gave a spectral resolution of $1.02\ \text{\AA}$ at $1200\ \text{\AA}$, $0.90\ \text{\AA}$ at $1500\ \text{\AA}$ and $0.84\ \text{\AA}$ at $1700\ \text{\AA}$. Similarly, the G230L grating had a dispersion of $1.58\ \text{\AA}/\text{pixel}$ yielding a spectral resolution of $3.5\ \text{\AA}$ at $1700\ \text{\AA}$ and $3.3\ \text{\AA}$ at $2400\ \text{\AA}$.

All *HST* spectra were reduced with the standard CALSTIS pipeline software. Where appropriate, we used INTTAG to divide TIMETAG exposures into sub-exposures before applying the CALSTIS calibration. For the near-UV (G230L) observations, we found no reason to change the default settings. The G140L far-UV data, however, suffered from artifacts around the geocoronal Ly α line. This occurs because the sky lines are tilted, and the default parameters are not adequate to precisely describe this. Therefore, we adjusted the tilt to fit better the 2-d spectra and moved the background regions closer to the source spectrum. This greatly improved the Ly α extraction, although some small residuals are still visible.

The mean *HST* spectra are shown in Figures 1, 2 and 3.

2.2. CTIO 4 m Blanco

Optical spectroscopy was obtained on 2003 February 13–15 using the R-C grating spectrograph (RCS) on the 4 m Blanco telescope at the Cerro-Tololo Interamerican Observatory (CTIO). The KPGL1 grating was used with a wavelength coverage of $3600\text{--}6620\ \text{\AA}$. The combination of the $1.3\ \text{arcsec}$ slit width, a spectral dispersion of $0.95\ \text{\AA}/\text{pixel}$ and a spatial scale of $0.5\ \text{arcsec}/\text{pixel}$ gave a spectral resolution of $2.47\ \text{\AA}$. Initial data reduction used standard IRAF¹⁰ techniques for bias removal, flat fielding, and optimal extraction of the spectra.

The slit was rotated to include another star on the slit, and this was used for both relative flux calibration and relative wavelength calibration. Owing to technical difficulties, we were unable to intersperse the target observations with arc calibrations and so wavelength calibration was done only using HeNeAr arcs from the beginning of the first night, with subsequent offsets derived using absorption lines in the spectrum of the comparison star. The comparison star was calibrated relative to the spectrophotometric standard EG21 (Hamuy et al. 1992, 1994) using an observation taken at low airmass with a wide-slit. All object spectra were then calibrated relative to this.

The mean spectrum from both nights of observation is shown in Figures 1 and 2.

2.3. VLT

Optical spectroscopy was also obtained on 2003 February 7 and 2003 February 28 with the Very Large Telescope

¹⁰ IRAF is distributed by the National Optical Astronomy Observatories, which are operated by the Association of Universities for Research in Astronomy, Inc., under cooperative agreement with the National Science Foundation.

TABLE 1
LOG OF ULTRAVIOLET AND OPTICAL OBSERVATIONS USED IN THIS WORK.

Facility	Instrumentation	Start date	UT range	Total Obs. (s)
<i>IUE</i>	SWP	1990 Dec 29	17:39–00:59	26400
	SWP	1990 Dec 30	17:02–23:35	23580
	SWP	1991 Jan 6	15:49–21:59	22200
VLT	FORS2, 1400V	2003 Feb 7	04:26–08:15	12000
	FORS2, 600RI	2003 Feb 28	02:38–06:09	12000
CTIO 4 m	RCS, KPGL1	2003 Feb 14	06:17–09:31	10860
	RCS, KPGL1	2003 Feb 15	03:48–09:31	18600
<i>HST</i>	STIS, G140L	2003 Feb 18	20:06–21:13	4000
	STIS, G140L		21:20–22:35	4500
	STIS, G140L		22:43–00:06	4970
	STIS, G230L	2003 Feb 19	00:17–00:31	800
	STIS, G140L		00:53–01:59	4000
	STIS, G140L		02:07–03:22	4500
	STIS, G140L		03:29–04:52	4970
	STIS, G230L		05:04–05:17	800
Magellan	IMACS, 600	2003 Dec 14	07:30:06	900
	IMACS, 300	2003 Dec 15	07:08:10	1200

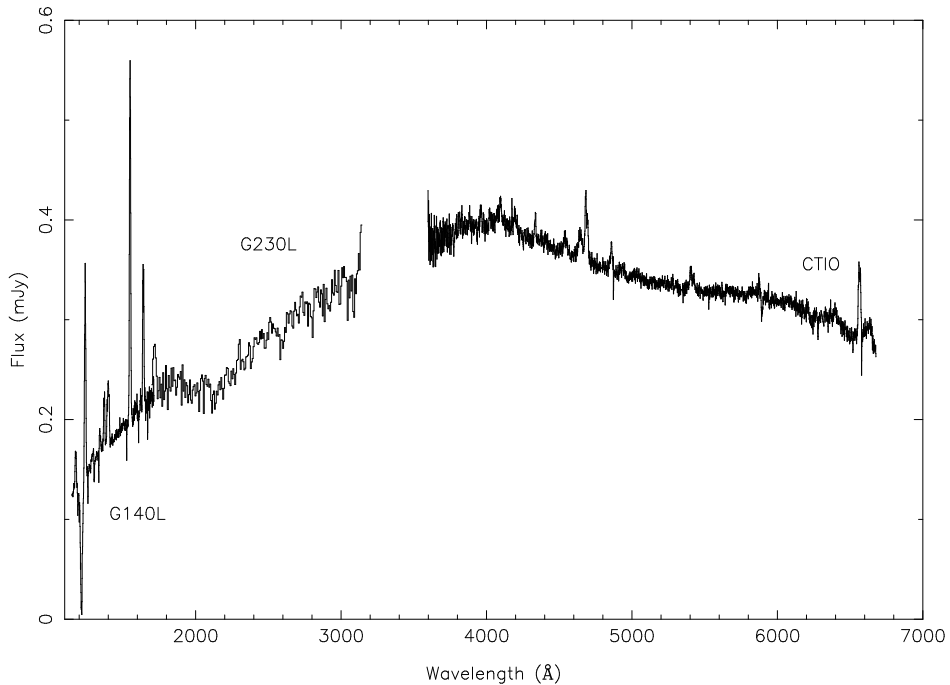


FIG. 1.— Compilation of the mean calibrated spectra from the HST and CTIO datasets.

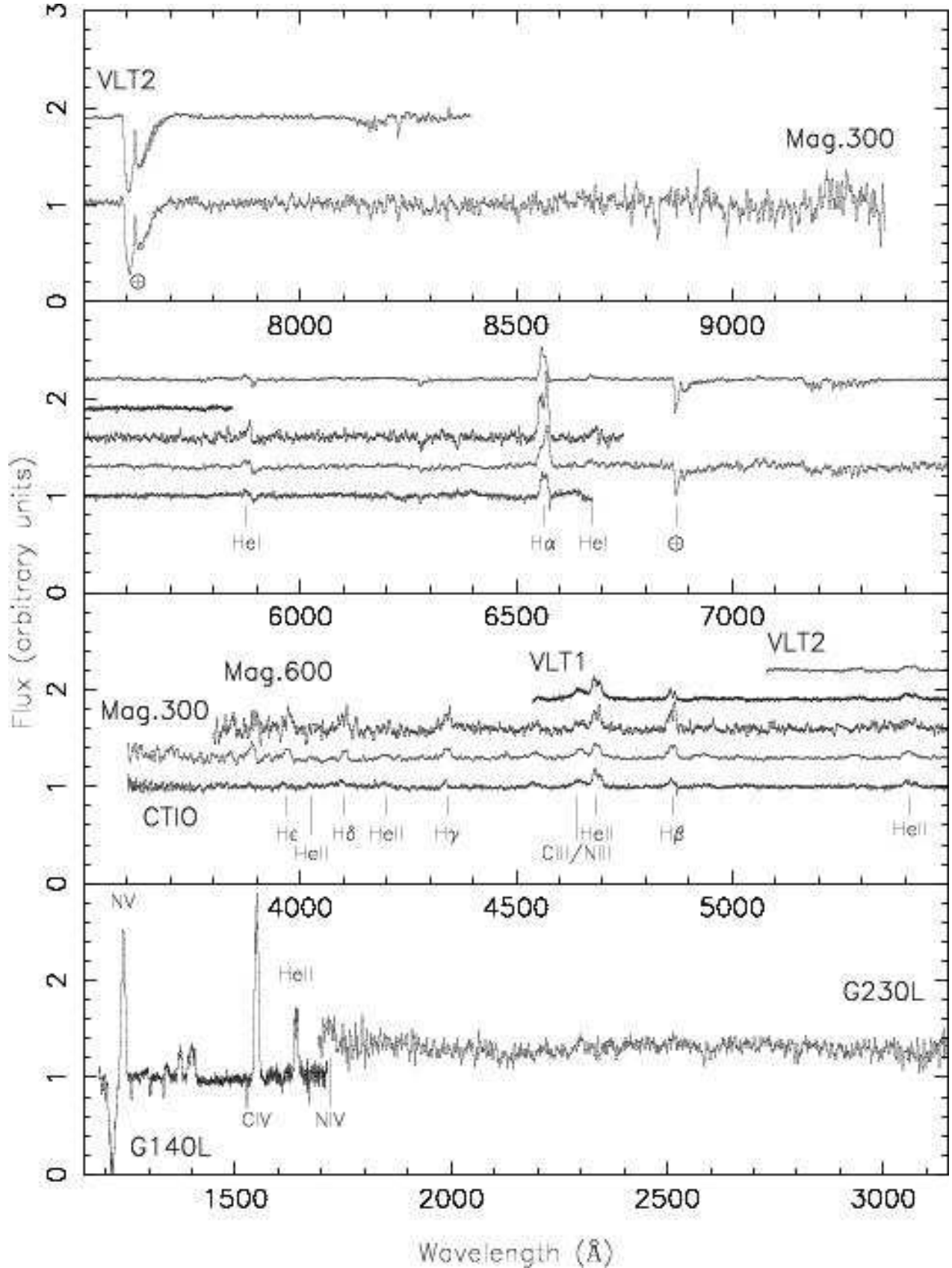


FIG. 2.— Compilation of all the spectra, normalised to unit continuum and offset, as necessary, by multiples of 0.3. Labels for all the lines in the G140 HST spectra are shown in Figure 3.

(VLT) at Cerro Paranal, Chile. The first night of observation used the FORS2 spectrograph and 1400V grating with wavelength coverage 4540–5840 Å and mean dispersion of 0.637 Å/pixel; the second night the 600 RI grating with 5080–8395 Å coverage and mean dispersion of 1.62 Å/pixel. Both sets of observations used a slit width of 0.4 arcsec, making slit losses significant and absolute flux calibration unreliable. With a spatial scale of 0.125 arcsec/pixel this gave a spectral resolution of 2.04 Å for night 1 and 5.18 Å for night 2.

Initial data reduction was again carried out using IRAF. He + Ne and HgCd arc lines were obtained during the day before and after the observations and interpolated through the night.

The mean spectrum from both nights of observation is shown in Figure 2.

2.4. Magellan

Two spectra were obtained with the 6.5 m Walter Baade, Magellan telescope at Las Campanas Observatory, Cerro Manqui, Chile on 2003 December 14/15. The IMACS instrument was used in f/4 configuration with a 0.7 arcsec slit and an 8k×8k CCD mosaic detector operating in 2×2 binning mode. The low-resolution spectrum was obtained using the 300 grating with a range of 3410–9350 Å and a 1.5 Å/pixel image scale giving 4.3 Å resolution. The higher-resolution spectrum was obtained using the 600 grating with a wavelength range of 3730–6830 Å, a 0.76 Å/pixel image scale and 2.0 Å resolution. Data reduction was carried out using PAMELA software. Both spectra are plotted in Figure 2.

2.5. Archival IUE spectra

Three spectra of EXO 0748–676 were obtained using the low-resolution short-wavelength prime camera (SWP) in 1990–1991. As these have not been published previously, we extracted the NEWSIPS reprocessed spectra (Nichols & Linsky 1996) from the archive for comparison with our new data. We constructed an exposure time weighted average. This is based on ~ 5 binary orbits and so should adequately represent the mean spectrum in 1990–1991. The extracted spectra are plotted alongside our *HST* spectra for comparison in Figure 3.

3. ANALYSIS AND DISCUSSION

3.1. Spectral characteristics

A broad range of emission lines are seen in the data, sampling a range of ionization stages and excitations. These are summarised in Table 2. In the optical, Balmer lines of H I are prominent alongside both He I and He II. The Bowen blend of N III and/or C III is clearly seen as in most LMXB spectra. The UV spectrum is also typical for an LMXB, being dominated by the strong lines of CIV and NV, alongside C III, N IV, O IV, and OV. The line strengths seen in the far-UV show no obvious anomalies and the ratio of CIV to NV is typical; there is no indication of substantial CNO processing as seen in XTE J1118+480, for example (Haswell et al. 2002).

In addition to emission, there are also absorption features. Broad Ly α absorption is common in all LMXBs, and may arise from the absorption in the disk atmosphere,

and/or the interstellar medium. Many metallic resonance absorption lines in the far-UV are also of interstellar origin. The Na D lines are only partially resolved in the CTIO data and also blended with He I limiting the precision with which their individual strengths can be measured. The total equivalent width is ~ 0.6 Å, with the D₂ line stronger than D₁. Assuming a ratio between 1:1 and 1:2, for D₁:D₂, implies a D₂ EW of 0.3–0.4 Å, and reddening $E(B - V)$ likely in the range 0.07–0.24 (Munari & Zwitter 1997). This is comparable to, but somewhat larger than, that deduced from the 2175 Å interstellar line in the forthcoming Paper III (Hynes et al., in prep.), $E(B - V) = 0.06 \pm 0.03$. The latter is probably a more reliable indicator. Both are markedly lower than the frequently quoted value of $E(B - V) = 0.42 \pm 0.03$ (Schoembs & Zoeschinger 1990), but this was based on an unreliable method for an LMXB, so our lower values are more credible. The final absorption components worthy of mention are moving features, present in the Balmer lines, that originate within the binary. These will be discussed more thoroughly in Section 3.3.

Equivalent widths were measured for all the lines in Table 2 in each dataset where they were present. The values are summarised in Table 3. Where there was significant phase coverage, each set of data was binned by phase with variance weighting and then a mean spectrum derived with equal weighting for each phase bin. Error estimates were derived by making the measurement 10 times with independently selected continuum regions in each case.

3.2. Lightcurves

Lightcurves were generated for several of the emission lines considered above having subtracted a polynomial fit to the local continuum in each case. These are plotted in Figure 4.

The CTIO H α data presents an overall smooth symmetric lightcurve. Surprisingly, this appears to have two peaks at $\phi = 0$ and 0.25 with a hint of brief absorption episodes either side of the former. The H β lightcurve also peaks around $\phi = 0$ but the rising part of the lightcurve appears steeper than the descending section. At minimum light, the flux completely disappears as a result of the absorption feature that moves across the line profile.

In contrast to the hydrogen Balmer lines, the He II 4686 Å line reaches a broad peak at around $\phi = 0.5$ and reaches a sharper minimum in the range $\phi = 0.9$ –0.0. The He II 1640 Å and He II 5412 Å lightcurves shows very little coherent behavior and much scatter and the C III 1176 Å lightcurve does not show any clear orbital modulation.

The 4 lightcurves NV 1240 Å, OV 1371 Å, Si IV 1400 Å and CIV 1549 Å show similar behavior. Each lightcurve peaks in the range $\phi = 0$ –0.1 and reaches a minimum around $\phi = 0.5$. However, the orbital modulation is relatively weak in each case. The material producing all 6 of the ultraviolet lines appears to be visible at all phases and uneclipsed. This suggests that rather than being distributed throughout the disk, these high ionization lines arise from specific regions that are never hidden by the secondary.

Crampton et al. (1986) published a broadband B lightcurve and 3 *equivalent width* line lightcurves. Their

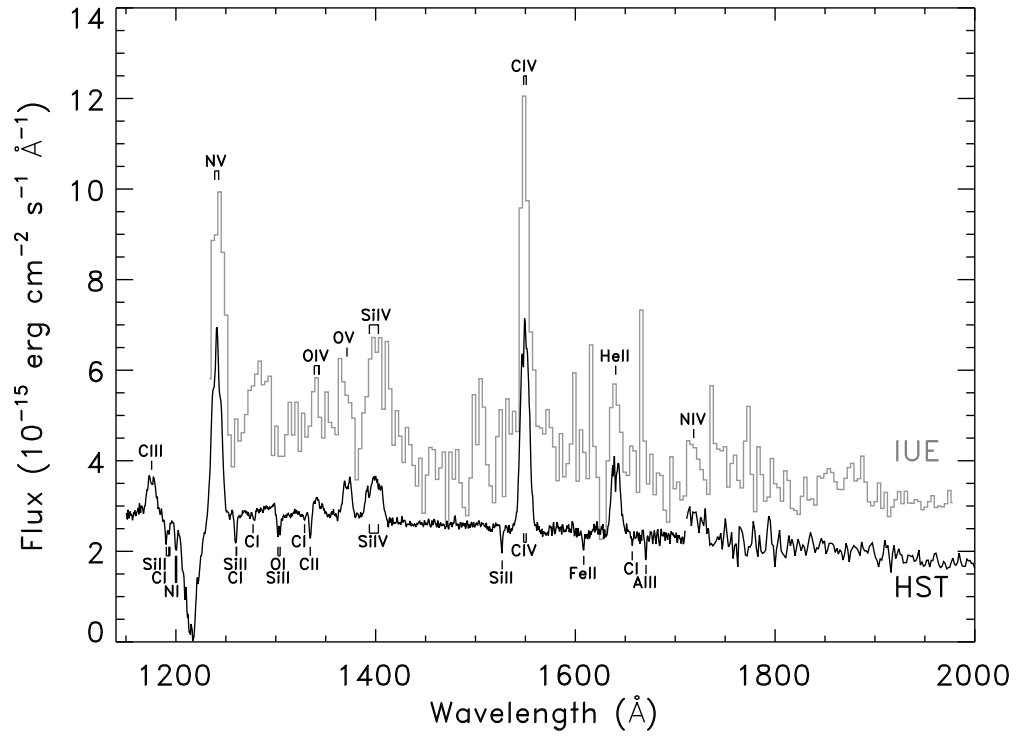


FIG. 3.— Mean IUE (1990–1991) and *HST* (2003) spectra.

TABLE 2

SUMMARY OF THE EMISSION LINES CONSIDERED IN THIS PAPER. NB. THE QUOTED IONIZATION ENERGY IS THAT REQUIRED TO *form* THE RELEVANT ION.

Line	Transition	E_{ion} (eV)	E_l (eV)	E_u (eV)
H α	2-3	—	10.20	12.09
H β	2-4	—	10.20	12.75
HeII 1640 Å	2-3	24.59	40.81	48.37
HeII 4686 Å	3-4	24.59	48.37	51.02
HeII 5412 Å	4-7	24.59	51.02	53.31
CIII 1176 Å	2s-2p	24.38	6.50	17.04
CIV 1549 Å	2s-2p	47.89	0.00	8.00
NV 1240 Å	2s-2p	77.47	0.00	9.99
OIV 1371 Å	2s-2p	77.41	19.69	28.73
SiIV 1400 Å	3s-3p	33.49	0.00	8.87

TABLE 3
THE MEASURED EQUIVALENT WIDTHS OF EMISSION LINES.

Line	EW(Å)					HST	Line
	VLT1	CTIO	VLT2	Mag. 300	Mag. 600		
H α	–	4.182(8)	4.930(38)	7.942(91)	12.966(18)	6.511(18)	HeII 1640 Å
H α w/o abs.	–	4.710(8)	5.165(10)	–	–	3.549(10)	CIII 1176 Å
H β	0.249(38)	1.008(11)	–	2.746(65)	4.061(94)	18.82(19)	CIV 1549 Å
H β w/o abs.	1.019(5)	1.273(10)	–	–	4.009(36)	16.52(10)	NV 1240 Å
HeII 4686 Å	4.607(23)	3.899(8)	–	4.662(38)	5.03(12)	2.212(4)	OV 1371 Å
HeII 5412 Å	1.597(7)	1.565(20)	1.462(5)	2.336(32)	1.870(21)	4.442(44)	SiIV 1400 Å

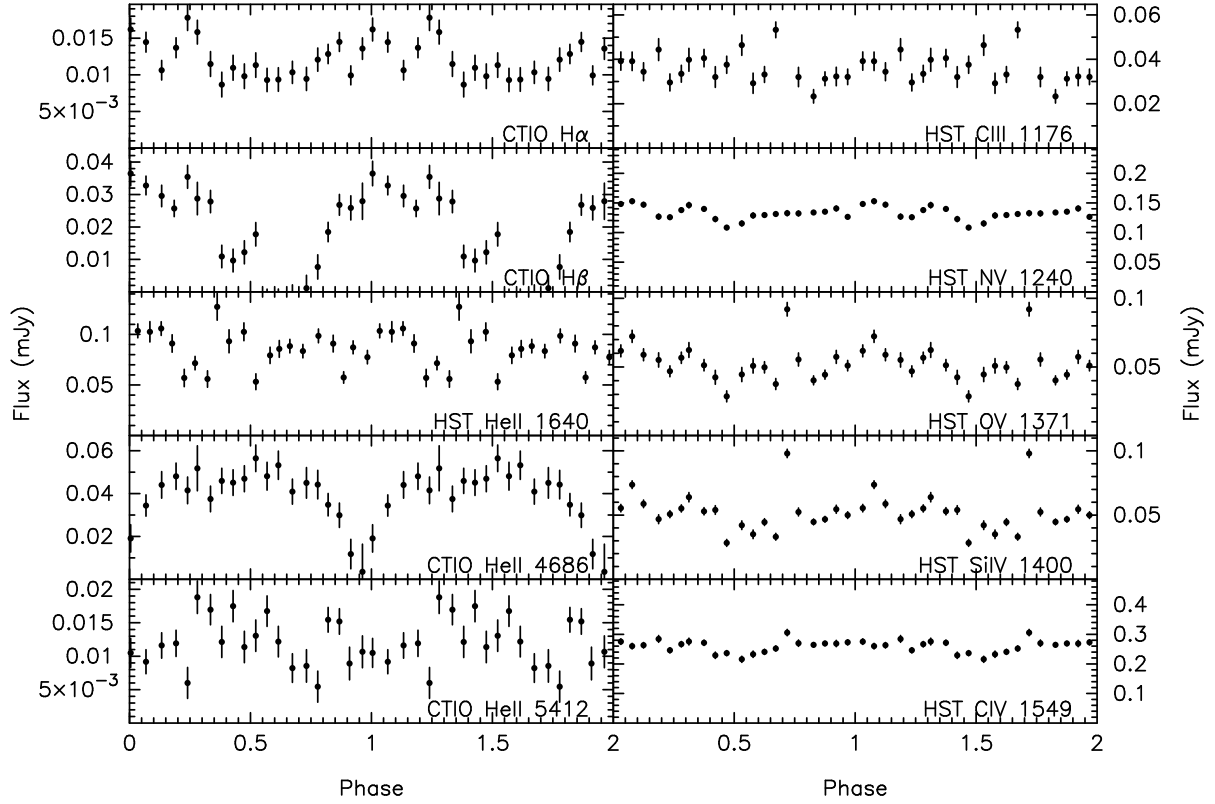


FIG. 4.— Lightcurves from the accurately calibrated spectra from the CTIO and HST datasets. The data has been phase binned in the range $0 < \phi < 1$ and is repeated for a second cycle.

$H\beta$ results are close to those presented here. However, their HeII 4686 Å plot contrasts strongly with ours; being similar to the $H\beta$ behavior. The HeII 4686 Å results derived from our CTIO data appear to be in anti-phase to this and eclipse in a similar way to the broadband lightcurve. Since the earlier results using equivalent width are effectively normalised to the continuum, their HeII 4686 Å lightcurve probably represent the behavior of the underlying continuum rather than the line behavior itself.

3.3. *Trailed Spectra*

Trailed spectra generated for all the emission lines considered above (summarised in Table 2) are given in Figures 5 and 6. The continuum in the region of each line was fitted with a low order polynomial and subtracted off. Normalising the flux by their continuum contributions before subtraction produced no significant differences in the results. The orbital phase was calculated using the ephemeris of Wolff et al. (2002). These data have all been binned by orbital phase and are shown over two cycles with some smoothing. A sine wave with an amplitude of 750 km s^{-1} has been over-plotted on each trail to guide the eye and aid in cross-comparisons. The amplitude was chosen to match the clearest observed S-wave which arises from the OV line.

The OV S-wave is so strong as to drown out the broader structures arising from the disk. The HeII 1640 Å line shows a clear hybrid structure with an S-wave matching the OV kinematics superimposed on a double peaked profile that arises from the accretion disk. Enhanced emission along the same sinusoid can also be identified in each of the remaining UV trails. The NV line is worthy of note as the S-wave appears superimposed on a constant velocity profile close to the line centre. This may arise from a double peaked disk profile where the blueward side has slumped into the $Ly\alpha$ absorption feature.

Looking closely at the $H\alpha$ and $H\beta$ trailed spectra, there seem to be two absorption components superimposed on the emission lines. An S-wave component is clear in the VLT2 $H\alpha$ data, less visible in the CTIO $H\alpha$ data and also in the phase range 0.5–1.0 for the two $H\beta$ datasets. In the $H\alpha$ data in particular, these align with the kinematics of the OV emission feature while the VLT1 $H\beta$ absorption traces a lower amplitude sinusoid. There is also a clear constant velocity component in the CTIO $H\beta$ data in the 0–0.4 range and possibly also in the VLT1 $H\beta$ and CTIO $H\alpha$ data.

Sample spectra showing the motion of the absorption features from the VLT datasets are shown in Figure 7. In an attempt to increase the signal to noise ratio, the $H\beta$ spectra are formed from an average of 4 individual observations leading to a degree of orbital smoothing.

In $H\alpha$, the absorption is clearly visible to the long wavelength side of the emission line at $\phi = 0.06$ and $\phi = 0.98$. At $\phi = 0.51$ the absorption is appearing on the blue side of the profile. At $\phi = 0.25$ and $\phi = 0.75$ the absorption is closer to the line center but predominantly affecting the red peak of the double peaked disk profile. In $H\beta$, the broad absorption feature is just apparent on the red wing at $\phi = 0.02$. The absorption moves into the double peaked disk profile and appears to be slightly to the blue side of

the line center at $\phi = 0.67$. By $\phi = 0.8$ the feature is moving back to the long wavelength side of the profile. This behavior is consistent with that shown by the only other two published spectra for this object that we are aware of (Crampton et al. 1986).

The similarity of the kinematics of the $H\alpha$ absorption and high ionization emission lines suggests that they arise from the same region. To achieve this would require the plasma to exist in both hot and cold phases simultaneously. Such a situation was envisioned in the overflowing stream model of Frank, King & Lasota (1987) with cold blobs embedded in a hotter low density gas. However, the temperatures required in that model are much higher than that which would produce the lines we observe. It is likely, therefore, that another mechanism is at work. For example, the temperature separation may arise from differences in the efficiency of cooling between denser and rarer regions. The velocity amplitude of the $H\beta$ absorption in the trailed spectra clearly changes between the VLT1 and CTIO observations. While the phase range 0.5–1.0 appears similar to the $H\alpha$ absorption, the constant velocity phases of the absorption requires a more complex explanation. With a velocity $\sim 650 \text{ km s}^{-1}$, this absorbing material has the correct velocity to be in Keplerian rotation at the circularization radius. However, it is more problematic to explain why different sections of any enhanced ring of material at this radius would be picked out with the observed phase dependence. Why, for example, do we see an S-wave absorption (from material in one region) at certain phases and then constant velocity absorption (implying material that is at that instant on the receding edge of the ring) at other phases? Qualitatively, we might understand the behavior as arising from an extended region of absorbing material along an overflowing stream. For early phases, the absorption would preferentially pick out that part of the stream obscuring the hottest (and thus brightest) part of the inner disk and consequently give rise to an approximately constant velocity component. This continues until we have passed the phase at which the point where the overflowing stream merges with the disk material no longer lies on a line between the observer and the neutron star. For the remaining phases the absorption traces out the S-wave appropriate to the merger point. Confirmation of this would require some reasonably sophisticated radiative transfer modelling. The behavior is also reminiscent of the simulated emission line kinematics produced by the method of Foulkes et al. (2004) in other as yet unpublished spectra. These models studied the eccentric, precessing accretion disks that give rise to superhumps in the SU UMa sub-group of DNe. Interestingly, the preferred mass ratio for this system ($q = 0.34$, see section 3.4.1 below) is right on the limit for which such eccentricity is possible. UU Aqr has the highest measured $q = 0.30$ for a superhumping system, whereas U Gem at $q = 0.36$ has only recently had a superhump period detected from a single outburst in 1985 (Baptista, Steiner & Cieslinski 1994; Smak 2001, 2002; Smak & Waagen 2004; Patterson et al. 2005). Confirmation of such an explanation would require similar modelling to be undertaken with parameters appropriate to EXO 0748–676.

Other systems also show absorption in the hydrogen Balmer lines but none with the same kinematics. The

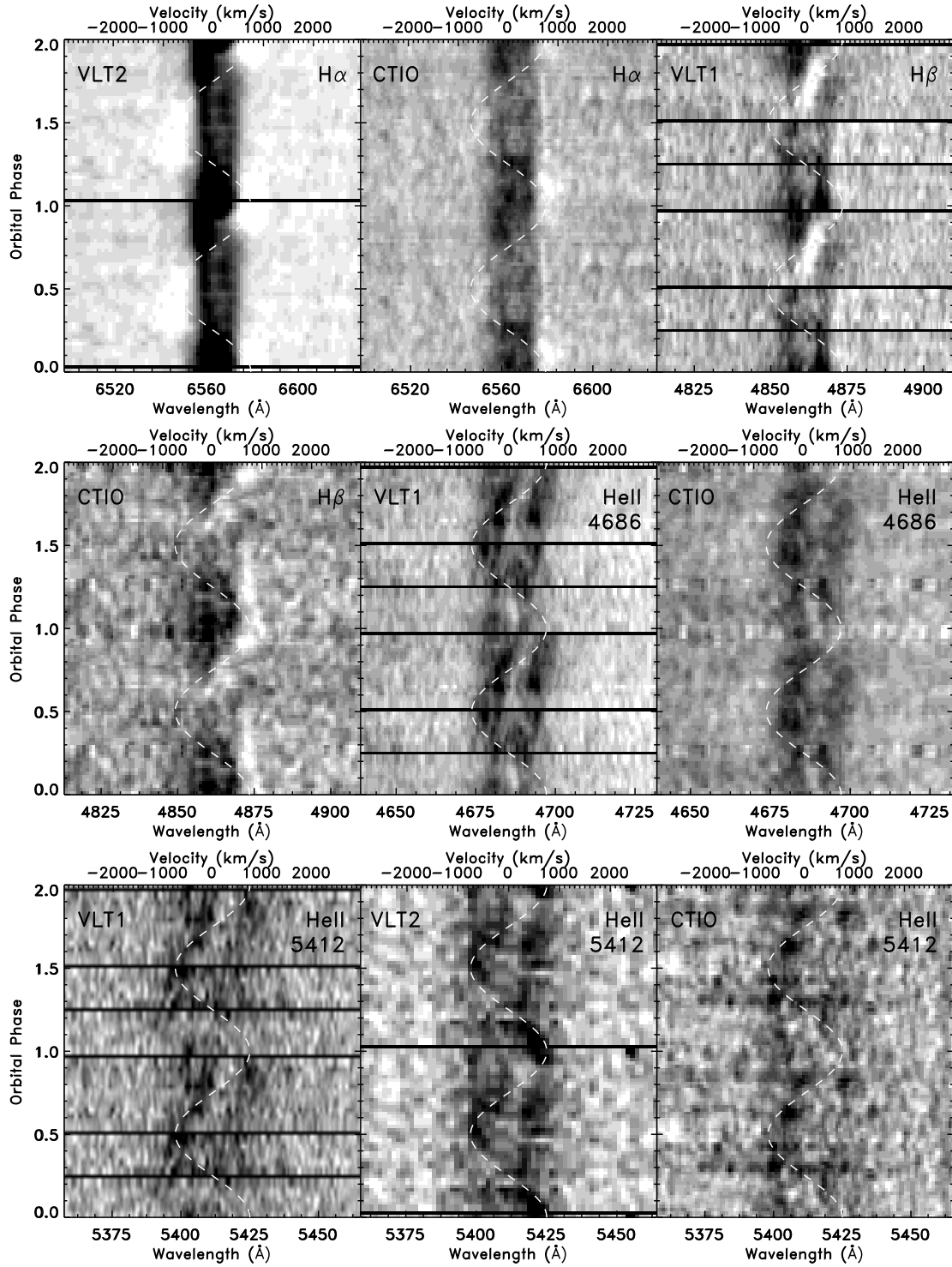


FIG. 5.— Trailed spectra of all of the considered optical emission lines. Each panel has a wavelength scale chosen to give a velocity range $\pm 3000 \text{ km s}^{-1}$ ($\frac{\Delta\lambda}{\lambda_0} = \pm 0.01$) and a sine wave of semi-amplitude 750 km s^{-1} have been over-plotted as a guide.

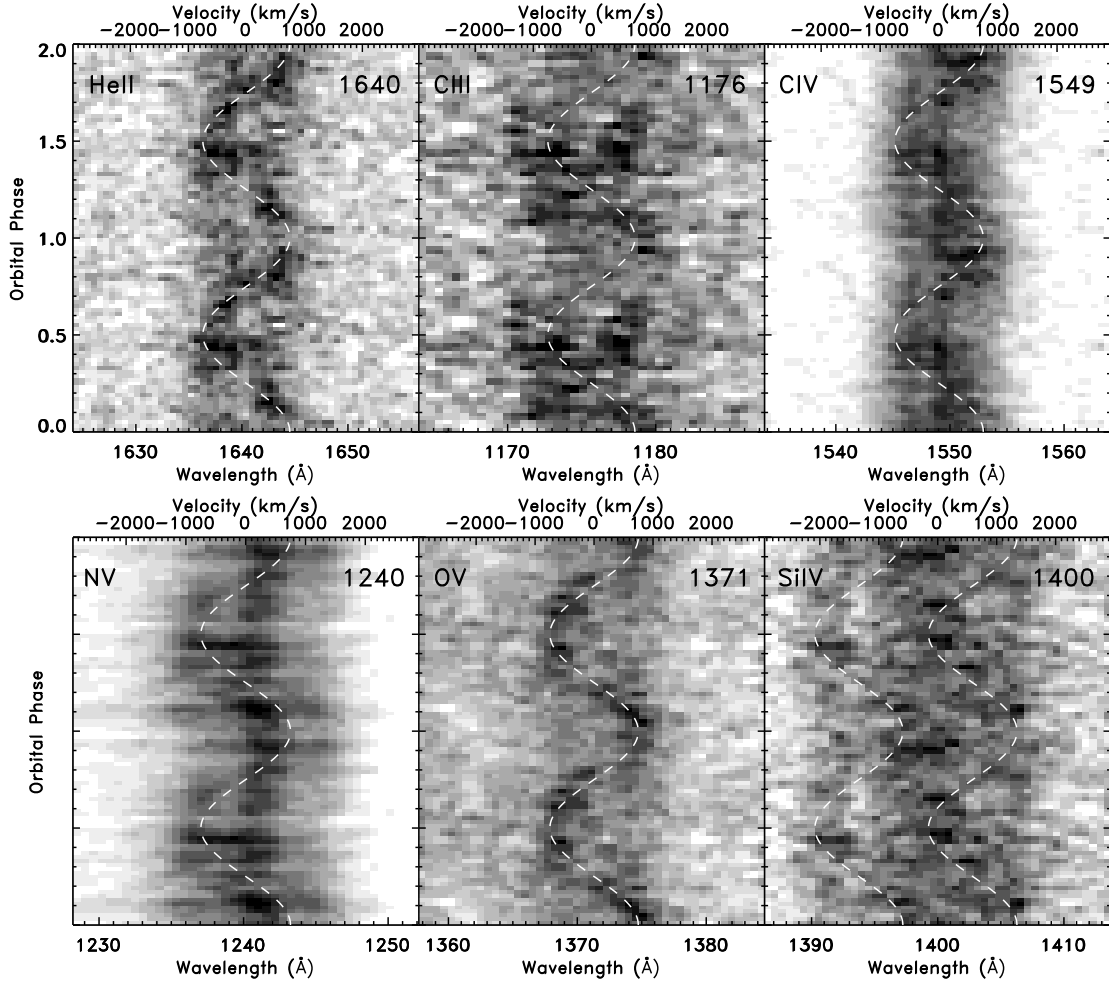


FIG. 6.— Trailed spectra of the considered ultraviolet emission lines. The wavelength scales have again been chosen to give a velocity range $\pm 3000 \text{ km s}^{-1}$ ($\frac{\Delta\lambda}{\lambda_0} = \pm 0.01$) and a sine wave of semi-amplitude 750 km s^{-1} have been over-plotted as a guide.

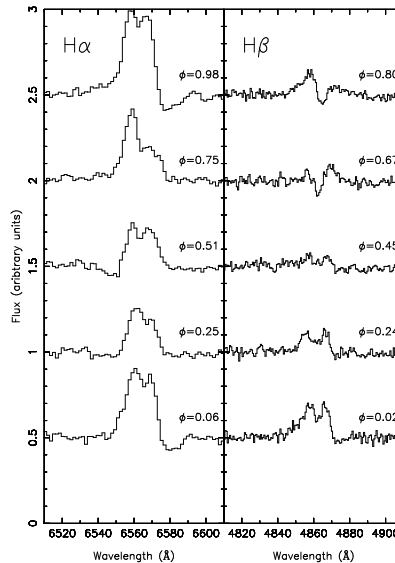


FIG. 7.— H α and H β spectra taken from the VLT datasets. Each spectrum has been normalised to unit continuum and offset in multiples of 0.5.

SW Sex systems are CVs which show the transient absorption during the approximate phase range 0.4–0.6 (Szkody & Piché 1990; Thorestensen et al. 1991; Warner 1995). Similarly, H α in the soft X-ray transient XTE J2123-058 shows transient absorption from 0.35–0.55. In both cases the absorption is generally interpreted as arising from stream material overflowing the disk (Warner 1995; Hynes et al. 2001). A contrasting LMXB system is 2A 1822-371 which shows broad absorption lines dominating and moving across the Balmer profiles in the approximate range $\phi = 0.5$ –1.0. Again, this is interpreted as arising from absorption by material in a vertically extended region resulting from a splash of material deflected around the hot spot (Casares et al. 2003).

Harlaftis, Charles & Horne (1997) measured a very weak FeII 6516 Å absorption feature in 2A 1822-371 at orbital phase 0.75. They ascribed this to the same “iron curtain” feature that was observed in OY Car by Horne et al. (1994). These earlier observations were taken in the ultraviolet using *HST* and showed a “forest of blended FeII features” that was interpreted as being due to material with supersonic, yet sub-Keplerian, velocity in the outer disk. Close examination of our optical and UV spectra show no convincing evidence for the presence of either feature in this system.

3.4. Doppler Tomograms

We have used the unsmoothed trailed spectra to generate Doppler tomograms using the maximum entropy technique of Marsh & Horne (1988). The tomograms formed from the optical observations are shown in Figure 8 and those from the *HST* observations in Figure 9. Markings on the plots were generated using $q = 0.34$, $M_1 = 1.35M_\odot$ and $i = 75.5^\circ$ (Model 3 of Paper I). The velocities of the centers of mass of the system and of the two stars are marked with crosses. The Roche lobe of the secondary and the Keplerian velocities at the expected edge of the disk and at the circularization radius are also plotted. Two trails are also indicated in the figure. The solid line shows the expected ballistic trajectory of material leaving the L1 point. The dot-dashed line shows the Keplerian velocity at each point that the ballistic stream would pass through.

The H α and H β lines show consistent behavior between both the CTIO and VLT datasets with emission confined to lower velocities than we would expect for any disk material. Both lines, however, suffer from the effects of the absorption feature that mean we must treat the derived tomograms with caution. Absorption violates an assumption in the reconstructive technique: that the observed flux is positive.

The HeII 4686 Å is similar in both VLT and CTIO datasets with emission close to the ballistic stream, although the CTIO tomogram has it in a position also consistent with the edge of the disk. The HeII 5412 Å tomograms are all rather noisy reflecting the weakness of the line and difficulty in effecting an accurate continuum subtraction. Although they all show scattered knots of emission about the disk, the lack of reproducibility strongly suggests that these are noise artifacts. Each of them, however, does show emission at some point along the ballistic stream.

The HeII 1640 Å line produces good results despite be-

ing far from the strongest line. The emission is spread out in a ring consistent with emission from a disk. Emission appears to extend along the stream in a similar way to the optical He line maps. Here, however, this emission region is significantly extended around the rim of the disk.

All of the ultraviolet maps from the *HST* dataset also show a ring of emission consistent with a disk. A possible exception is OV 1371 Å which appears to lack emission in the orbital phase range $\phi = 0.1$ –0.5. This may just be a relative deficit compared to the strong emission region. The NV 1240 Å line suffers from the interference of the Ly α adjacent absorption which is difficult to remove with great confidence. The more isolated CIV 1549 Å would seem a better bet for a good result but, unfortunately, the line consists of two components separated by the equivalent $\sim 500 \text{ km s}^{-1}$. Convolved with the double peaked disk profile this leaves a difficult dataset to disentangle and gives rise to the filling in of emission at low velocity. The CIII 1176 Å, OV 1371 Å and SiIV 1394,1403 Å lines are all weaker, with the latter also sharing the complication of being a doublet. While the reconstruction routine does allow such doublet lines to be specified with their relative strengths there is inevitably a loss of information in such an entangled case.

The high points of emission in the CIII 1176 Å map all occur along the projected ballistic stream deep into the disk. The line is extremely weak and so potentially unreliable, however.

The high excitation line SiIV 1400 Å, CIV 1549 Å, NV 1240 Å and OV 1371 Å tomograms all show emission in the phase range $\phi \sim 0.65$ –0.75. The latter two lines, with higher, but almost equal, ionization potentials, appear to come from further into the disk. None of this emission lies along the continuation of the ballistic stream or the Keplerian velocity corresponding to the stream position as envisioned by the overflowing stream model. However, it is consistent with the region downstream of the hot spot impact and/or the early part of a stream overflow.

The SiIV 1400 Å tomogram is similar to that from HeII 1640 Å. Strong emission sites are scattered around the disk rim although no emission appears along the stream.

Given the velocity resolution of the data, it is difficult to say with certainty whether the strong emission sites in the tomograms occur at velocities significantly different from that expected at the disk rim. The most reliable maps in this regard would be those from the first VLT dataset for HeII 5412 Å and HeII 4686 Å. In these maps, there is emission in the stream region. The former also shows emissions sites close to the circularization velocity. These maps, along with that for CIII 1176 Å, all hint that the stream may be overflowing the disk.

We might, alternatively, attempt to explain the velocity of the emission being in an area we would associate with disk material in terms of a thick rim model. If the disk were puffed up by X-ray irradiation, it would be natural to expect high ionization lines to appear near the rim. However, contemporaneous X-ray observations in Paper III show dips at a wide range of phases. Indeed, similar to the results of Bonnet-Bidaud et al. (2001), only the ranges $\phi = 0.2$ –0.3 and $\phi = 0.45$ –0.55 show a *lack* of dipping activity. Given azimuthal disk symmetry (or some close approximation) why would one particular phase be sin-

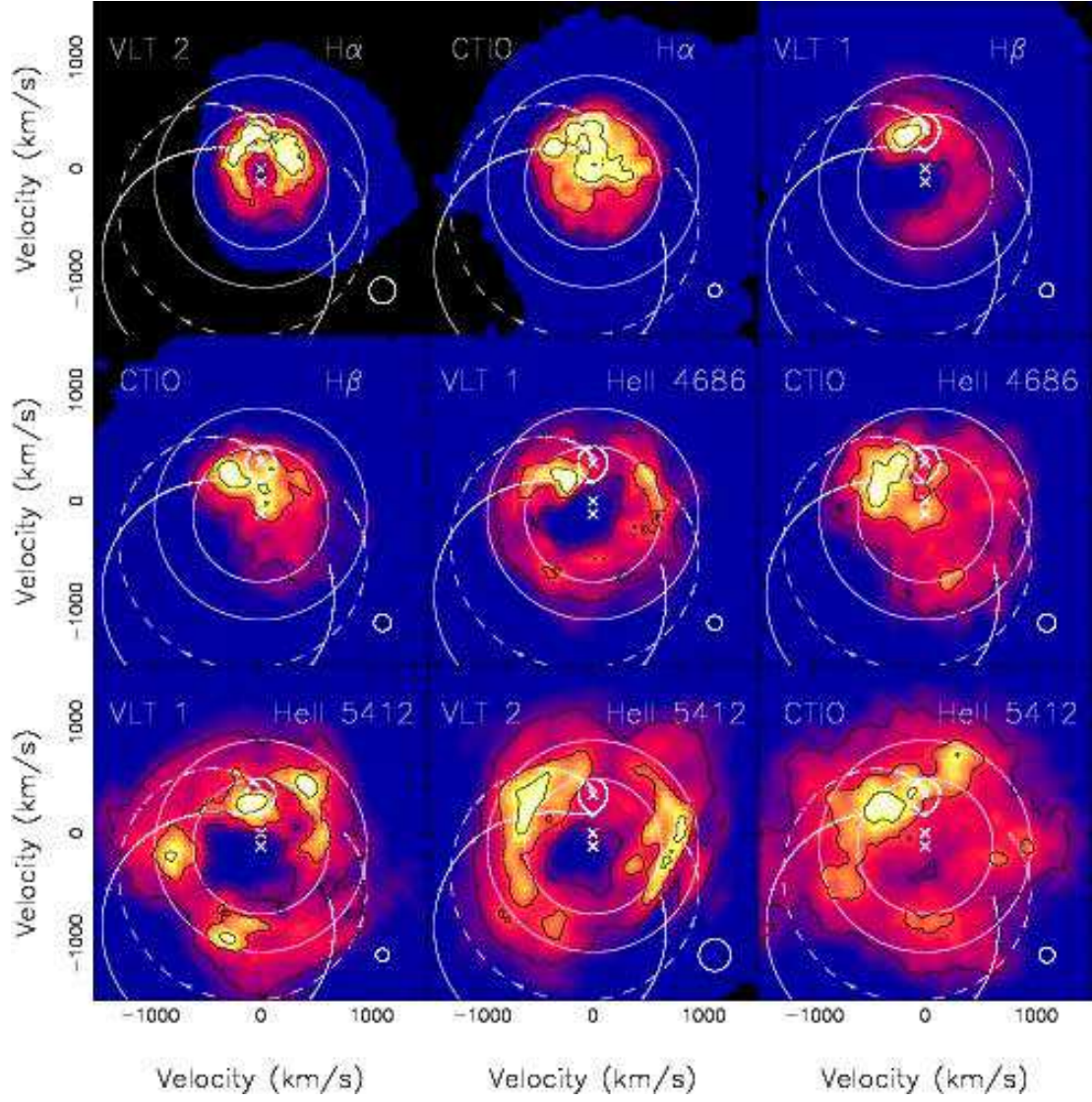


FIG. 8.— Tomograms formed from the CTIO and VLT data. The expected track of material leaving the L1 point and travelling ballistically is marked by a solid line. The Keplerian velocity at each point along that track is plotted as a dot-dashed line. The secondary's Roche lobe, the velocity of the primary and the Keplerian velocities at the expected position of the edge of the disk and at the circularization radius are also plotted. The circle in the bottom right of each panel has a diameter equal to the velocity resolution of the data.

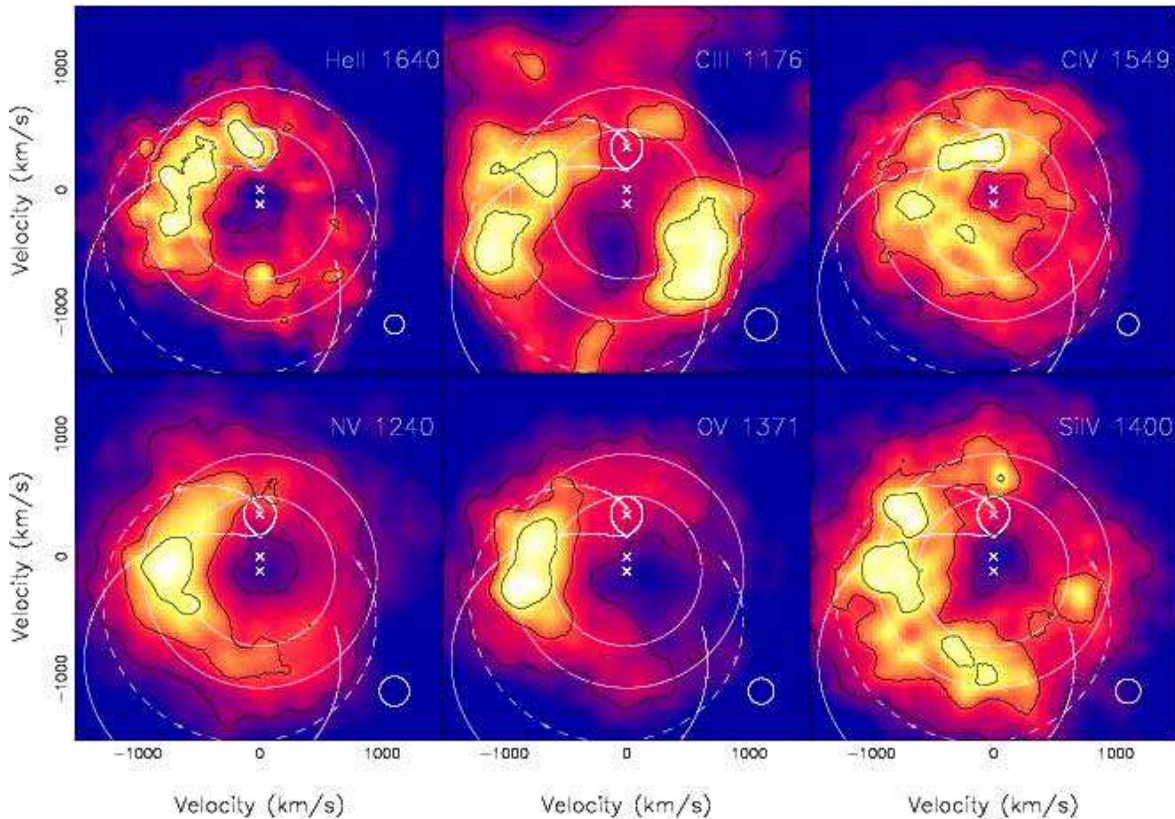


FIG. 9.— Tomograms formed from the *HST* data. Again a circle has been plotted in each panel with a diameter equal to the velocity resolution of the data.

gled out for emission? In the overflowing stream model, this can be attributed to the different physical conditions that exist along the stream and in each region of the disk with which it interacts with increasing ionization as the central star is approached.

3.4.1. Constraining the Mass-ratio q

We can compare the same Doppler tomograms with tracks generated using different choices for the q, i pairs allowed by the observed eclipses. This is useful as it is often possible to constrain further the acceptable range of q (and hence i) to those consistent with identifiable features, in particular the stream. We would expect the stream emission to arise at velocities between the ballistic and Keplerian value along the stream trajectory. The tomogram formed from the VLT1 observations of the HeII 4686 Å line are shown in Figure 10 with markings generated for a selection of M_2 values. For $M_1 = 1.35M_\odot$, these appear to favour values of M_2 at the high end of the range considered in Paper I and the observations are most compatible with the assumption of a main sequence secondary ($M_2 = 0.46M_\odot$, $i = 75.5^\circ$, Model 3). Özel (2006) recently proposed a lower limit $M_1 > 2.1M_\odot$. However, in that case the Model 3 ballistic trajectory barely passes through the strong emission region. To achieve the same degree of agreement as for $M_1 = 1.35M_\odot$, we would require $M_2 \approx 0.84M_\odot$ (plotted as Model 4), approximately 80% more massive than a main sequence companion. Schenker & King (2002) showed how an overmassive secondary can arise as the result of mass transfer stripping away the sec-

ondary’s envelope to reveal a helium rich core. However, the example they give only has a maximum mass excess of around 40% and then only for $M_2 < 0.1M_\odot$, significantly smaller in both parameters than we would require. These difficulties led us to retain the assumption of a main sequence secondary with $1.35M_\odot$ primary as the choice for the markings in Figures 8 and 9 above.

4. CONCLUSIONS

Stepping back from the details, we can attempt to identify the common features present in the dataset, focusing on the highest quality lines. Beginning with the tomograms, these appear to show two components across several lines. Firstly a ring of emission is present that can likely be associated with the accretion disk (or a coronal layer above it). Secondly, excess emission is usually present on the left hand side of the tomogram. In HeII 4686 Å, this is in the upper left quadrant and consistent with the accretion stream and/or impact point, with the implied disk radius consistent with tidal truncation. In the higher ionization resonance lines, most obviously OV and NV, this is preferentially lower in the tomogram, below the ballistic stream. This suggests emission from material carried downstream in the disk from the initial stream-impact. HeII 1640 Å appears as a hybrid of the two extremes. The velocities of the high excitation lines are lower than expected from a purely ballistic stream overflow, but appear higher than expected from material at the disk rim; they are intermediate between Keplerian velocities at the disk rim and the circularization radius, suggesting that

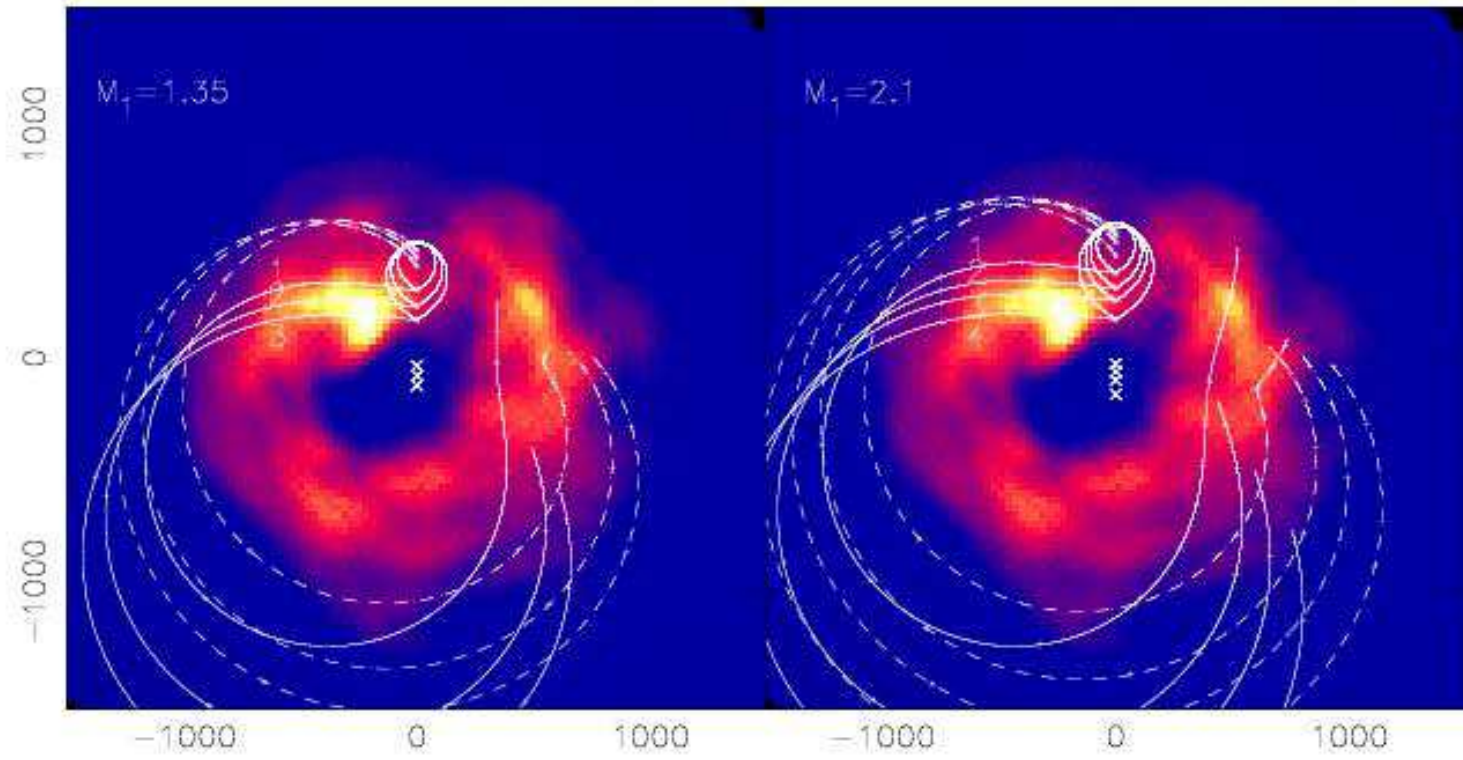


FIG. 10.— Doppler tomogram of the VLT1 observation of the HeII 4686 Å line. Markings are calculated for the different values of q and i appropriate to the three models considered in Hynes et al. (2006a): $M_2 = 0.11M_\odot$ (Model 1); $M_2 = 0.27M_\odot$ (Model 2) and $M_2 = 0.46M_\odot$ (Model 3). The left-hand panel assumes $M_1 = 1.35M_\odot$ and the right-hand panel $M_1 = 2.1M_\odot$. The latter also has markings for a new Model 4, calculated for $M_2 = 0.84M_\odot$.

some penetration of the disk is occurring. Lightcurves provide support for this trend. HeII 4686 Å, which appears to originate at the stream-impact point in the tomograms, is deeply eclipsed as expected, whereas the UV lines including HeII 1640 Å, which appear to originate from downstream of the stream-impact point, show no eclipses. Comparison of the stream position in the Doppler tomograms to models supports the hypothesis that the secondary is a main sequence star and the system has a mass ratio of 0.34.

Examining the trailed spectra, the OV line provides the clearest S-wave component, and appears to show least disk emission. Its S-wave can be clearly seen in trailed spectra of other lines when one allows for their multiplet structure where appropriate. Most surprising is that the same S-wave appears to trace out *absorption* in the Balmer lines. While it is not required that gas with the same velocity be co-spatial, if it is this points to a two-phase medium. Cool material will produce low ionization absorption lines when backlit by hotter underlying material, whereas the hot component will produce high ionization emission lines, as observed. The presence of this component in H α at high velocities at both phases 0.0 and 0.5 in the VLT2 trailed spectrum indicates that absorption cannot simply be by the disk rim but must be by material above the disk, as the rim will not be backlit at $\phi = 0.5$.

The picture that thus emerges is that the accretion stream impacts the disk and some material overflows or penetrates it, albeit with velocities closer to the disk rim

than to a purely ballistic overflow. The overflowing material forms a two-phase medium. The densest clumps remain relatively cool and produce low ionization absorption of the brighter background disk, whereas the lower density material is hotter and produces high ionization emission.

This work includes observations with the NASA/ESA *Hubble Space Telescope*, obtained at STScI, which is operated by AURA Inc. under NASA contract No. NAS5-26555. Support for *HST* proposal GO 9398 was provided by NASA through a grant from STScI. RIH acknowledges support from NASA through Hubble Fellowship grant #HF-01150.01-A awarded by STScI.

Data from the NASA/ESA/SERC International Ultraviolet Explorer were obtained from the Multimission Archive at the Space Telescope Science Institute (MAST). Support for MAST for non-HST data is provided by the NASA Office of Space Science via grant NAG-7584 and by other grants and contracts. *IUE* data were obtained as part of the *ROSAT-IUE* All Sky Survey, by proposal M1180 (PI Penninx).

DS acknowledges a Smithsonian Astrophysical Observatory Clay Fellowship.

We are very grateful to Tim Abbott for assistance in mitigating technical difficulties with the CTIO 4 m. This work has made use of the NASA Astrophysics Data System Abstract Service.

We thank Tom Marsh for the use of MOLLY and PAMELA software packages.

REFERENCES

- Armitage, P. J., Livio, M. 1996, *ApJ*, 470, 1024
 Baptista, R., Steiner, J. E., Cieslinski, D. 1994, *ApJ*, 433, 332
 Bonnet-Bidaud, J. M., Haberl, F., Ferrando, P., Bennie, P. J., Kendziorra, E. 2001, *A&A*, 365, L282
 Casares, J., Steeghs, D., Hynes, R. I., Charles, P. A., O'Brien, K. 2003, *ApJ*, 590, 1041
 Crampton, D., Cowley, A. P., Stauffer, J., Ianna, P., Hutchings, J. B. 1986, *ApJ*, 306, 599
 D'Avanzo, P., Campana, S., Casares, J., Israel, G. L., Covino, S., Charles, P. A., Stella, L. 2005, *A&A*, in press (astro-ph/0508583)
 Flannery, B. P. 1975, *MNRAS*, 170, 325
 Frank, J., King, A. R., Lasota, J.-P. 1987, *A&A*, 178, 137
 Foulkes, S. B., Haswell, C. A., Murray, J. R., Rolfe, D. J. 2004, *MNRAS*, 349, 1179
 Harlaftis, E. T., Charles, P. A., Horne, K. 1997, *MNRAS*, 285, 673
 Hamuy, M., Walker, A. R., Suntzeff, N. B., Gigoux, P., Heathcote, S. R., & Phillips, M. M. 1992, *PASP*, 104, 533
 Hamuy, M., Suntzeff, N. B., Heathcote, S. R., Walker, A. R., Gigoux, P., & Phillips, M. M. 1994, *PASP*, 106, 566
 Haswell, C. A., Hynes, R. I., King, A. R., & Schenker, K. 2002, *MNRAS*, 332, 928
 Horne, K., Marsh, T. R., Cheng, F. H., Hubeny, I., Lanz, T. 1994, *ApJ*, 426, 294
 Hynes, R. I., Charles, P. A., Haswell, C. A., Casares, J., Zurita, C., Serra-Ricart, M. 2001, *MNRAS*, 324, 180
 Hynes, R. I., et al. 2006a, in press (astro-ph/0605143) (Paper I)
 Hynes, R. I., et al. 2006b, in prep. (Paper III)
 King, A. R., Kolb, U., Szuszkiewicz, E. 1997, *ApJ*, 488
 King, A. R. 2006, Chapter 13, in: "Compact Stellar X-ray Sources", Ed: Lewin, W., van der Klis, M., Cambridge University Press, Cambridge, in press (astro-ph/0301118)
 King, A. R., Cannizzo, J. K. 1998, *ApJ*, 499, 348
 Lubow, S. H., Shu, F. H. 1975, *ApJ*, 198, 383
 Lubow, S. H., Shu, F. H. 1976, *ApJ*, 207, L53
 Marsh, T. R., Horne, K. 1988, *MNRAS*, 235, 269
 Mason, K. O., et al. 1980, *ApJ*, 242, L109
 Munari, U., & Zwitter, T. 1997, *A&A*, 318, 269
 Nichols, J. S., Linsky, J. L. 1996, *AJ*, 111, 517
 Özel, F. 2006, *Nature*, in press (astro-ph/0605106)
 Patterson, J. et al. 2005, *PASP*, 117, 1204
 van Paradijs, J. 1996, *ApJ*, 464, L139
 van Paradijs, J., van der Klis, M., Pedersen, H. 1988, *A&AS*, 76, 185
 Parmar, A. N., White, N. E., Giommi, P., Haberl, F., Pedersen, H. 1985, *IAU Circ.*, 4039
 Parmar, A. N., White, N. E., Giommi, P., Gottwald, M. 1986, *ApJ*, 308, 199
 Proffitt, C., et al. 2002, *STIS Instrument Handbook*, Version 6.0, STScI, Baltimore
 Schenker, K., King, A. R. 2002, in: "The Physics of Cataclysmic Variables and Related Objects", Eds. Gänsicke, B. T., Beuermann K., Reinsch K., ASP Conference Series, 261, 243
 Schoembs, R., Zoeschinger, G. 1990, *A&A*, 227, 105
 Smak, J. I. 2001, *Acta Astron.*, 51, 279
 Smak, J. I. 2002, *Acta Astron.*, 52, 189
 Smak, J. I., Waagen, E. O. 2004, *Acta Astron.*, 54, 433
 Steeghs, D., Casares, J. 2002, *ApJ*, 568, 273
 Still, M. D., Quaintrell, H., Roche, P. D., Reynolds, A. P. 1997, *MNRAS*, 292, 52
 Szkody, P., Piché, F. 1990, *ApJ*, 361, 235
 Thorestensen, J. R., Ringwald, F. A., Wade, R. A., Schmidt, G. D., Norsworthy, J. E., 1991, *AJ*, 102, 272
 Torres, M. A. P., Casares, J., Martínez-Pais, I. G., Charles, P. A. 2002, *MNRAS*, 334, 233
 Torres, M. A. P., Callanan, P. J., Garcia, M. R., 2003, *MNRAS*, 341, 1231
 Torres, M. A. P., Callanan, P. J., Garcia, M. R., Zhao, P., Laycock, S., Kong, A. K. H. 2004, *ApJ*, 612, 1026
 Vrtilik, S. D., Quaintrell, H., Boroson, B., Still, M., Fiedler, H., O'Brien, K., McCray R. 2001, *ApJ*, 549, 522
 Wade, R. A., Quintana, H., Horne, K., Marsh, T. R. 1985, *PASP*, 97, 1092
 Warner B. 1995, *Cataclysmic Variable Stars*, Cambridge Univ. Press, Cambridge
 White, N. E., Holt, S. S. 1982, *ApJ*, 257, 318
 White, N. E., Nagase, F., Parmar, A. N. 1995, Chapter 1, in: "X-Ray Binaries", Eds. Lewin, W. H. G., Van Paradijs, J., Van den Heuvel, E. P. J., CUP, Cambridge
 Wolff, M. T., Hertz, P., Wood, K. S., Ray, P. S., Bandyopadhyay, R. M. 2002, *ApJ*, 575, 384